Imaging Characteristics of a Highly Integrated Millimeter Wave MIMO Radar

Simon Kueppers*, Siying Wang*, Harun Cetinkaya*, Reinhold Herschel*, Nils Pohl**

*Fraunhofer Institute for High Frequency Physics and Radar Techniques FHR
Wachtberg, Germany
email: simon.kueppers@fhr.fraunhofer.de

**Institute for Integrated Systems, Ruhr University Bochum
Bochum, Germany

Abstract: *In this paper the influence of antenna radiation pattern on the imaging performance of a highly integrated Millimeter Wave Radar is presented. For evaluation of the MIMO imaging performance the implemented antenna array topology is shown and using an analytical antenna model the simulated point spread function is given for different antenna half-power beamwidths. Simulated and measured characterization of a circularly polarized cavity backed patch antenna on a Rogers® RT/duroid 5880 substrate implemented in a compact radar system is presented. The experimental evaluation of the imaging performance is carried out by comparing simulation and measurement of a scenario with multiple point-like scatterer using the realized antenna element.*

1. Introduction

The integration of radar modules on silicon has enabled the miniaturization of complex radar imaging devices. Multi-channel radar is not exclusively available for large military setups, but can now be integrated in complex sensor suites for robotics or industrial sensing [1]. Several integrated radar modules have been developed mainly addressing E-Band for automotive applications [2, 3] or the license free ISM-Bands [4, 5]. The higher the frequency of operation, the higher the achievable level of integration for a given frequency. Especially for small distances millimeter wave radar technology can shrink module sizes to several centimeters still maintaining reasonable imaging quality.

At Fraunhofer FHR a highly compact radar module was developed with a size of $50\,\text{mm} \times 40\,\text{mm} \times 30\,\text{mm}$ within the Horizon2020 project SmokeBot. The module is based on SiGe MIMO technology [6] and completely includes millimeter wave frontend and backend so that data and configuration can be exchanged easily using a standard Ethernet interface [7]. However, the small number of 2×8 transmit and receive channels results in a significant limitation by sidelobes which can be reduced by focusing of the single antenna elements. This was simulated and realized in hardware to allow angular estimation of arrival within the field of view using a minimum number of channels.

978-3-7369-9545-1

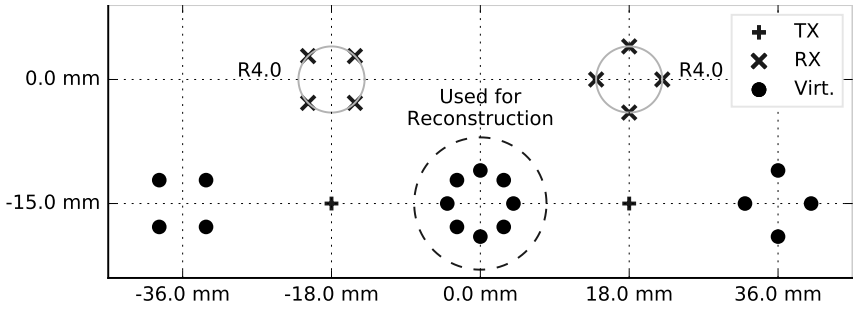

Figure 1: Realized MIMO antenna topology and resulting virtual antenna array

The paper will first introduce the antenna array design followed by simulation the point spread function of the radar for different antenna half-power beamwidths. This is followed by a detailed analysis of the designed antenna element as well as the simulated and measured characteristics of the implemented antenna. The imaging performance simulations are finally verified by imaging experiments using the realized module.

2. MIMO Antenna Array Topology

For imaging purposes, a novel planar 2D sparse MIMO array using 2×8 transmitters and receivers has been developed for 3D imaging purposes and published in [8]. As shown in Fig. 1, eight receiving antennas are split up into a pair of four and are located on the same vertical axes as each of the two transmitting antennas. The resulting two receiver clusters are rotated by 45° with respect to each other such that the inter-element spacing is reduced from $2.4\lambda_c$ to $1.2\lambda_c$ in the resulting virtual antenna array. This alleviates the spatial requirements forced upon a single antenna element on the frontend circuit board and allows easier frontend design with respect to the antenna feed wiring. In the virtual array three separate clusters of virtual elements can be observed, however the data from the outermost clusters is discarded for data processing.

3. Imaging Performance

It is expected that the radiation pattern of the individual antenna elements affects the imaging characteristics of the MIMO radar. In the following this impact is simulated based on the array's point spread function as well as typical imaging scenarios. To analyze the focusing characteristics of the antenna array, a point spread function is simulated with different antenna half power beamwidths. In the simulation a point target is placed at 1 m distance and a 3D point spread function is reconstructed with the backprojection algorithm [9]. The rectangular reconstruction volume has a size of 200 cm × 200 cm × 100 cm with a voxel size of 1 cm. A Gaussian-shaped model is used to simulate the radiation pattern, which is described by Eq. 1

$$G = \exp(-a \cdot (1 - \cos(\vartheta)^2)) \qquad \vartheta \in [0, \frac{\pi}{2}], \quad \varphi \in [-\pi, \pi] \tag{1}$$

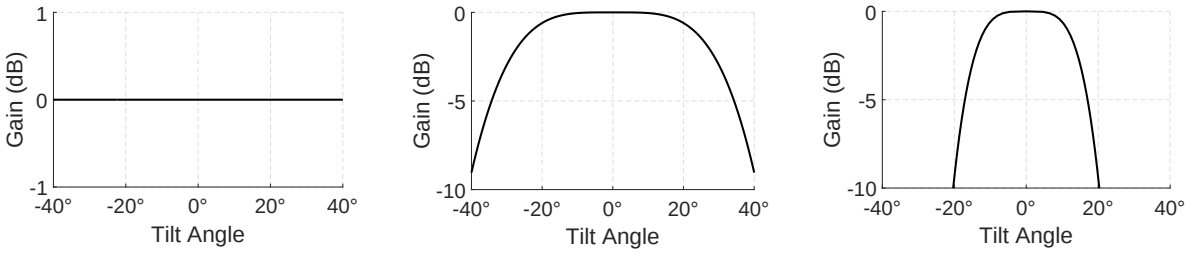

(a) Isotropic Antenna (b) HPBW: 60° (c) HPBW: 30°

Figure 2: Radiation Pattern with different half power beamwidths

In this simplified model it is assumed that the gain function is identical for every angle φ, hence it is rotationally symmetric around the Z-axis giving a good approximation to the implemented antenna element. The constant a determines the beamwidth of the radiation pattern. Fig. 2 shows the gain function for an isotropic antenna element and for antennas with a half-power beamwidth of 60° and 30°, respectively.

In Fig. 3, Fig. 4 and Fig. 5 the front-view, top-view, and side-view of the reconstructed 3D point spread function are displayed for the different beamwidths using the antenna topology shown in Fig. 1. In case of an isotropic radiation pattern the front-view in Fig. 3a shows the main lobe at the center, the circular side lobes at −8 dB and the grating lobes around the side lobe at −4 dB. The grating lobes are caused by the sparse antenna positioning due to the low number of antenna elements. The side lobes are caused by the circular distribution of the virtual antenna elements. In Fig. 4a and Fig. 5a the top-view and side-view are displayed and it can be seen that the side lobes and grating lobes are located between the antenna array and the point target, therefore the side lobes and grating lobes can be misinterpreted as target objects in the near range area.

Furthermore in Fig. 3 to Fig. 5 the point spread function imaging results are shown for antenna elements with a half power beamwidth of 60° and 30°. The −3 dB cross range resolution of the main lobe is 15 cm for all three antenna characteristics (Fig. 2). Different to near field imaging the individual antenna characteristics do not affect the image resolution in this case. For an antenna with 60° HPBW the grating lobes are not visible any more (see Fig. 3b) and are suppressed to below −15 dB, but a side lobe ring at −10 dB is still recognizable. In Fig. 3c which shows the 30° HPBW case the side lobe ring also decreases to below −15 dB. In the top-view (Fig. 4c) and side-view (Fig. 5c) images for 30° HPBW, the position of the point spread function can be distinctly detected at 1 m distance with a range resolution of 1.25 cm. The advantage of using antennas with narrower beamwidths for this sparse antenna array are the reduction of side lobes and grating lobes. However, the disadvantage is the restriction in field-of-view when choosing smaller beamwidths. Hence, there is a trade-off between side lobe suppression and field-of-view for a given antenna array topology, which should be taken into consideration when choosing the antenna beamwidth. In this specific case the beamwidth was chosen to be similar to the field of view of a camera using a half-power beamwidth of 30°.

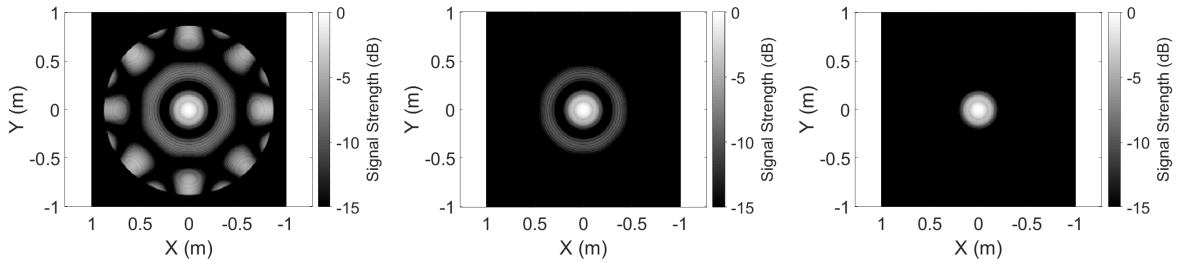

(a) Isotropic Antenna (b) HPBW: 60° (c) HPBW: 30°

Figure 3: Front-view (2D-image in XY-view with maximum value in Z-direction)

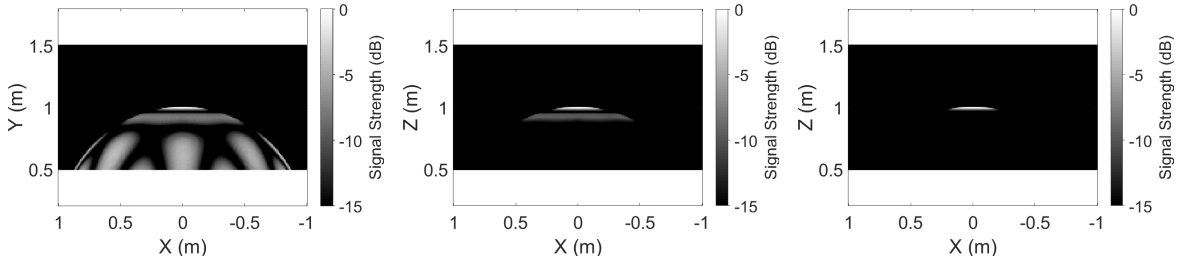

(a) Isotropic Antenna (b) HPBW: 60° (c) HPBW: 30°

Figure 4: Top-view (2D-image in XZ-view with maximum value in Y-direction)

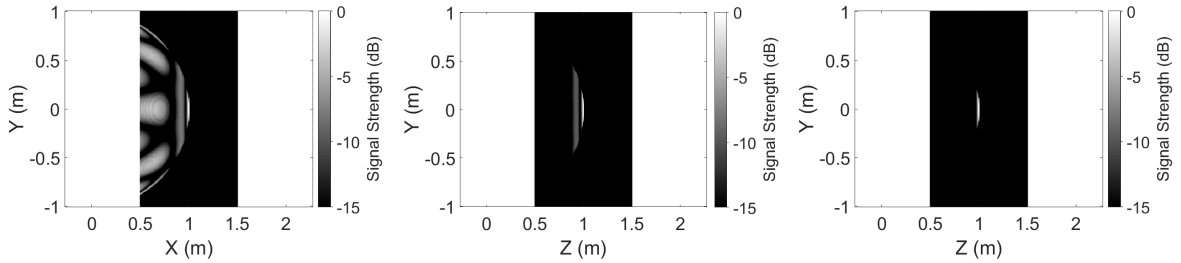

(a) Isotropic Antenna (b) HPBW: 60° (c) HPBW: 30°

Figure 5: Side-view (2D-image in ZY-view with maximum value in X-direction)

4. Antenna Element Design

With respect to the implemented multistatic MIMO radar system, several different considerations have gone into the development of the antenna as the main radiating and receiving element. Firstly the antenna beamwidth should satisfy the requirements posed by the requirements outlined in the previous section and only illuminate the desired field-of-view aiding to reduce clutter produced by grating lobes of strong scatterers outside the field-of-view. Secondly, the antenna element should be simple in design and easy to manufacture on a single 127 µm Rogers® RT/duroid 5880 substrate layer with a top layer and a ground plane so that there is no need for expensive manufacturing of complex multilayered circuit boards.

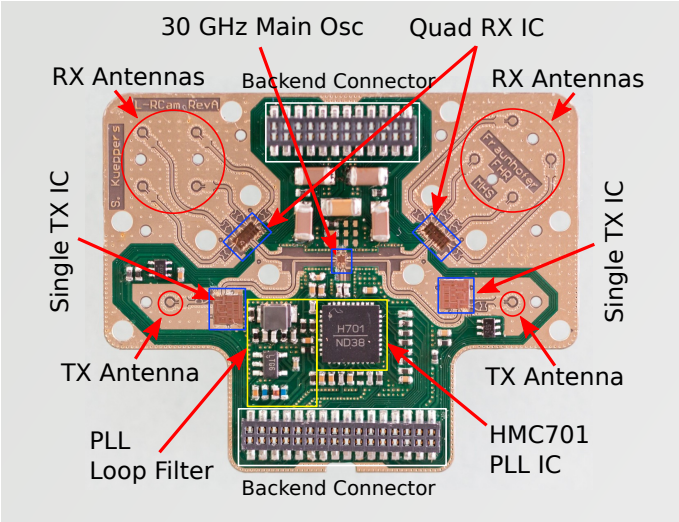

Figure 6: Radar system frontend circuit board with components from [7]

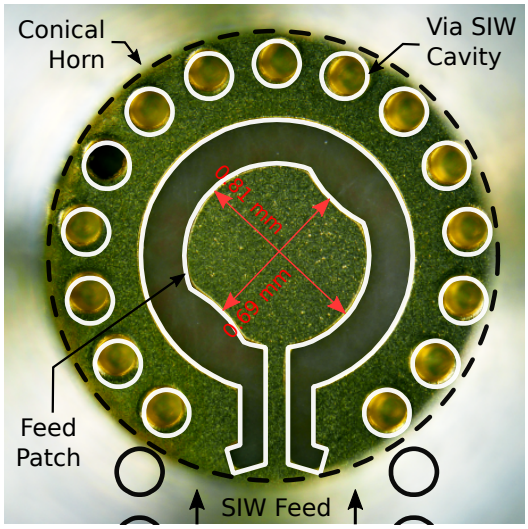

Figure 7: Top metallization of antenna element realized

While the design of linear polarized antennas typically used in similar radar systems [10, 11] is straightforward, we propose the use of circular polarized antennas for the antenna topology. This approach has two main advantages as described in the following. In time-multiplexed MIMO radar systems only a single transmitter circuit is transmitting at any time during the data acquisition. However, due to the imperfect isolation of the receiver downconversion mixer's local oscillator port to its RF port, each receive channel leaks some amount of local oscillator power. This converts every receiver circuit into a weak transmitter resulting in additional clutter showing up in the reconstructed data. To suppress the clutter generated by the leaked local oscillator signal circular polarized antennas are used so that all receiving antennas provide a circular polarization with an opposite rotational polarization to the transmitting antennas. The second advantage of using circularly polarized radiating elements are the reduced requirements regarding polarization fading. Thus, the receive and transmit antenna alignment can be arbitrary thus further simplifying the spatial requirements forced upon a compact frontend design.

The antenna element realized in this work is shown in Fig. 7. As it can be seen, a non-symmetric patch backed by a substrate integrated waveguide cavity similar to the design published in [12] has been realized. The patch dimensions have been determined using CST® Microwave Studio such that an impedance match and a good axial ratio at a center frequency of 122.5 GHz was achieved. However, since planar antennas typically exhibit a broad radiation pattern in both radiation planes, a conical horn was used to achieve a 35° half-power beamwidth to match the desired field-of-view of the antenna topology. The horn structure has been integrated into the frontend enclosure that is also protecting the electronic circuits. A substrate integrated waveguide feed for the cavity backed patch antenna was chosen to allow the enclosure containing the conical horn structure to be mounted directly onto the top copper layer without the need of gaps for microstrip or coplanar waveguide feedlines.

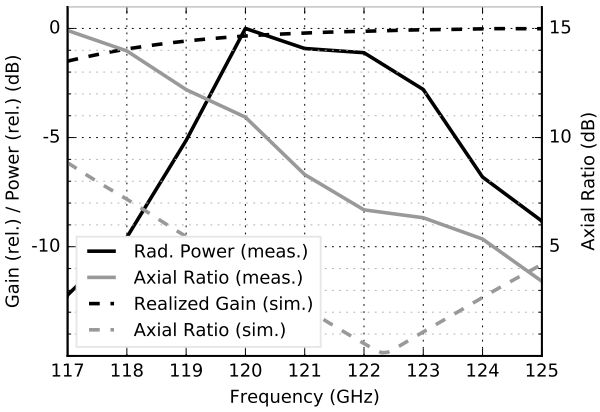

Figure 8: Simulation and measurement of antenna gain, radiated power and axial ratio over frequency

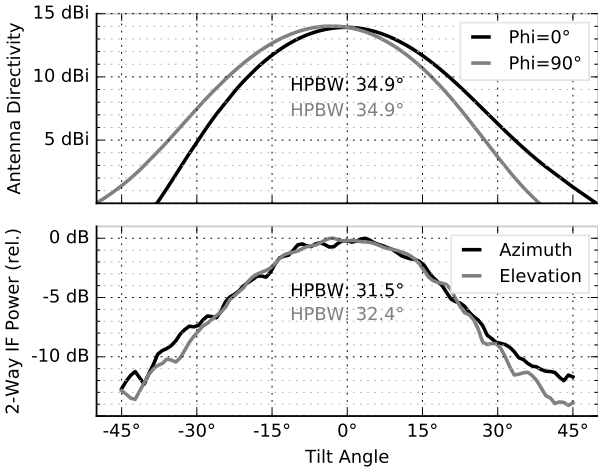

Figure 9: Simulated radiation pattern of antenna and measured 2-way IF power level over tilt angle

The dashed lines in Fig. 8 show the simulated realized gain and axial ratio of the main lobe as a function of operating frequency. The realized antenna gain is flat in the frequency range of interest and the axial ratio reaches 0 dB at 122.3 GHz, increasing to either direction on the frequency axis. The solid lines show the measured performance of a single transmitter element measured using a linear polarized receiver horn antenna connected to a spectrum analyzer. The black line shows the maximum power radiated while the transmit antenna has been rotated along the axis of its main lobe direction. As can be seen, the frequency dependency of the radiated power is much stronger compared to the simulation of the single antenna element. However it should be noted that the radiated power is influenced not only by antenna directivity and efficiency but also by the amplitude flatness of the power being fed to the antenna. The maximum radiated power was measured at frequencies between 120 – 123 GHz dropping off to either side of the frequency band.

Additionally Fig. 8 shows the ratio of the maximum and minimum power measured along the mainlobe direction (solid grey line). The measured axial ratio shows the same slope as the simulated curve. However the frequency of minimum axial ratio is achieved outside of the maximum tunable frequency range of the radar frontend. This is probably related to manufacturing tolerances in the circuit board production. For comparison of the imaging performance of the radar system, the optimum axial ratio could not be realized. However, the polarization dependency does not affect the imaging characteristics determined by the antenna array topology. The resulting reduction in signal-to-noise ratio from the polarization fading was not a limiting factor in the test scenarios chosen.

In the top plot in Fig. 9 the simulated radiation pattern of a single antenna element in main lobe direction as a projection on two orthogonal planes perpendicular to the direction of radiation is shown. As can be seen the simulated half power bandwidth is 34.9° in each plane and the beam is slightly tilted in one plane. A simulated antenna directivity of 14 dBi can be observed in the main

lobe direction. The bottom plot in Fig. 9 shows the measured two-way radiation pattern using the IF data acquired with a 119 – 123 GHz frequency sweep. The radar system has been pivoted in two orthogonal planes effectively measuring the corresponding antenna radiation planes of the simulation. The measured amplitudes of a trihedral reflector from all 16 channels have been summed up for each measurement point to allow the presentation of the achieved illuminated field-of-view. From this measurement the effectively illuminated half-power beamwidths of 31.5° and 32.4° have been calculated, showing close relation to the simulated values of the single antenna element.

5. Experimental Evaluation

For analyzing the imaging characteristics in a real measurement setup, a metal bar was placed in 1 m distance and a corner reflector in 1.5 m distance from the 2D MIMO array plane (Fig. 10).

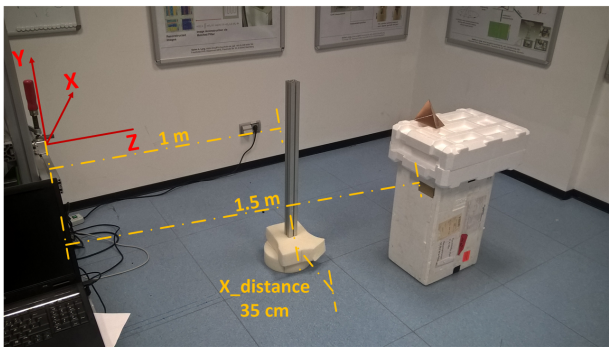

Figure 10: Measurement Setup (Metal Bar and Corner Reflector)

The distance between the two targets is 35 cm and the antenna array is located at the center between the two targets. The measurement is performed with a center frequency of 117 GHz and a bandwidth of 12 GHz. The same setup is simulated with a rectangular surface of 4 cm $\times$ 100 cm representing the metal bar and a point target is used to simulate the corner reflector. The measured

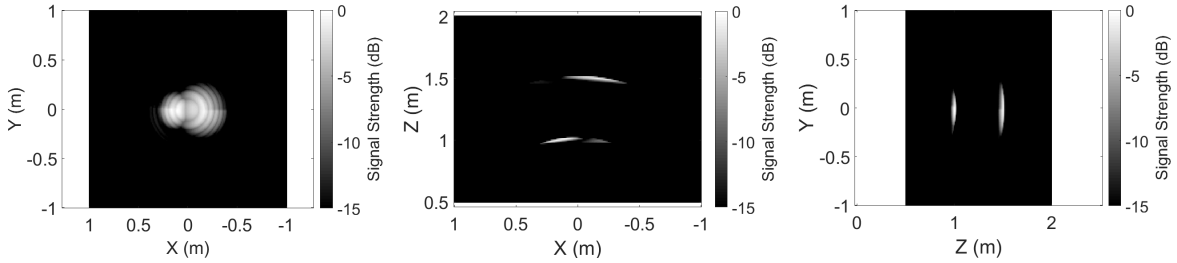

(a) Front-view (b) Top-view (c) Side-view

Figure 11: Simulation (Metal Bar and Corner Reflector)

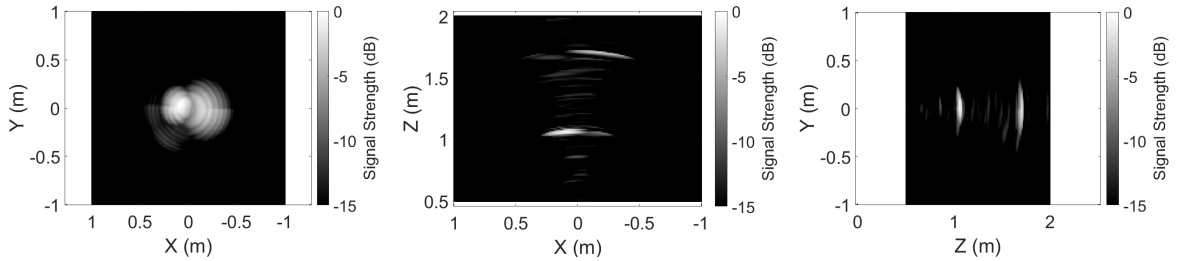

(a) Front-view (b) Top-view (c) Side-view

Figure 12: Measurement (Metal Bar and Corner Reflector)

2-Way IF Power from Fig. 9 showing a HPBW of 32.4° is included as radiation pattern for the simulation and it is also considered in the image reconstruction algorithm. In Fig. 11 and Fig. 12 the 3D image results from the measured and simulated data are compared.

In the front-view (Fig. 12a) an overlap of the two target objects is visible. The metal bar is an ideal reflector and because of the limited size of the antenna array the strongest reflection comes from the boresight direction, hence the metal bar is visible as a point target in the frontview image overlapping with the point spread function of the corner reflector. The same effect can be seen in the simulated image result (Fig. 11a). The two targets can be very well distinguished and located in the top-view and side-view image. In the measured results additional artifacts are visible (see Fig. 12b and Fig. 12c), which are probably caused by ground and multipath reflections. These artifacts are not considered in the simulation where an ideal surrounding is assumed. Despite the additional artifacts the target objects are clearly distinguishable.

6. Conclusion

In this paper the impact of the single antenna element characteristics on MIMO imaging performance has been presented. Following the introduction of the MIMO antenna array topology simulations comparing different antenna beamwidths have been presented that show a distinct dependence of imaging performance on the characteristics of a single antenna element. Following the simulated results the implemented antenna used in the system has been included along with its measured radiation pattern showing good agreement with the simulated result. The realized antenna element can be easily manufactured even in high quantities. In order to verify the simulated imaging performance a scenario with two point-like targets has been setup and measured. The corresponding simulation has been realized using an analytical antenna model. The measurement of the test-scenario shows good agreement with the simulated results. In the chosen scenario with the realized half power beamwidth and a field-of-view of 32.4° of the antenna element the side lobes and grating lobes have been sufficiently suppressed to detect and distinguish a two target object as has been verified by the measured data.

Acknowledgment

This work has partly been supported within H2020/ICT by the European Commission under grant agreement number 645101 (SmokeBot).

References

[1] P. Fritsche, S. Kueppers, G. Briese, and B. Wagner, "Radar and LiDAR Sensorfusion in Low Visibility Environments," in *Proceedings of the 13th International Conference on Informatics in Control, Automation and Robotics - Volume 2: ICINCO*, 2016, pp. 30–36.

[2] N. Pohl, T. Jaeschke, and K. Aufinger, "An Ultra-Wideband 80 GHz FMCW Radar System Using a SiGe Bipolar Transceiver Chip Stabilized by a Fractional-N PLL Synthesizer," *IEEE Transactions on Microwave Theory and Techniques*, vol. 60, no. 3, pp. 757–765, March 2012.

[3] R. Feger, C. Wagner, S. Schuster, S. Scheiblhofer, H. Jager, and A. Stelzer, "A 77-GHz FMCW MIMO Radar Based on an SiGe Single-Chip Transceiver," *IEEE Transactions on Microwave Theory and Techniques*, vol. 57, no. 5, pp. 1020–1035, May 2009.

[4] E. Öztürk, D. Genschow, U. Yodprasit, B. Yilmaz, D. Kissinger, W. Debski, and W. Winkler, "A 60-GHz SiGe BiCMOS Monostatic Transceiver for FMCW Radar Applications," *IEEE Transactions on Microwave Theory and Techniques*, vol. 65, no. 12, pp. 5309–5323, Dec 2017.

[5] H. J. Ng, M. Kucharski, W. Ahmad, and D. Kissinger, "Multi-Purpose Fully Differential 61- and 122-GHz Radar Transceivers for Scalable MIMO Sensor Platforms," *IEEE Journal of Solid-State Circuits*, vol. 52, no. 9, pp. 2242–2255, Sept 2017.

[6] S. Kueppers, K. Aufinger, and N. Pohl, "A Fully Differential 100-140 GHz Frequency Quadrupler in a 130 nm SiGe:C Technology for MIMO Radar Applications using the Bootstrapped Gilbert-Cell Doubler Topology," in *2017 IEEE 17th Topical Meeting on Silicon Monolithic Integrated Circuits in RF Systems (SiRF)*, Jan 2017, pp. 37–39.

[7] S. Kueppers, H. Cetinkaya, and N. Pohl, "A Compact 120 GHz SiGe:C based 2 x 8 FMCW MIMO Radar Sensor for Robot Navigation in Low Visibility Environments," in *2017 14th European Radar Conference*, 2017.

[8] H. Cetinkaya, S.Kueppers, R. Herschel, and N. Pohl, "Focusing Patterns within Far and Near Field for a Novel 2D Sparse MIMO Array," in *2017 14th European Radar Conference*, 2017.

[9] S. S. Ahmed, A. Schiessl, and L. P. Schmidt, "Multistatic mm-Wave Imaging with Planar 2D-Arrays," in *2009 German Microwave Conference*, March 2009, pp. 1–4.

[10] D. Bleh, M. Rösch, M. Kuri, A. Dyck, A. Tessmann, A. Leuther, S. Wagner, B. Weismann-Thaden, H. P. Stulz, M. Zink, M. Rießle, R. Sommer, J. Wilcke, M. Schlechtweg, B. Yang, and O. Ambacher, "W-Band Time-Domain Multiplexing FMCW MIMO Radar for Far-Field 3-D Imaging," *IEEE Transactions on Microwave Theory and Techniques*, vol. PP, no. 99, pp. 1–11;, 2017.

[11] S. S. Ahmed, A. Schiessl, and L. P. Schmidt, "A Novel Fully Electronic Active Real-Time Imager Based on a Planar Multistatic Sparse Array," *IEEE Transactions on Microwave Theory and Techniques*, vol. 59, no. 12, pp. 3567–3576, Dec 2011.

[12] D. Y. Kim, J. W. Lee, T. K. Lee, and C. S. Cho, "Design of SIW Cavity-Backed Circular-Polarized Antennas Using Two Different Feeding Transitions," *IEEE Transactions on Antennas and Propagation*, vol. 59, no. 4, pp. 1398–1403, April 2011.